

# Evaporation and Propagation of Liquid Drop Streams at Vacuum Pressures, Experiments and Modeling

D. R. Guildenbecher, J. J. Barnard, T. W. Grasser, A. M. McMaster, R. B. Campbell, D. P. Grote, P. Nandy, M. Light

July 13, 2020

Physical Review E

# Disclaimer

This document was prepared as an account of work sponsored by an agency of the United States government. Neither the United States government nor Lawrence Livermore National Security, LLC, nor any of their employees makes any warranty, expressed or implied, or assumes any legal liability or responsibility for the accuracy, completeness, or usefulness of any information, apparatus, product, or process disclosed, or represents that its use would not infringe privately owned rights. Reference herein to any specific commercial product, process, or service by trade name, trademark, manufacturer, or otherwise does not necessarily constitute or imply its endorsement, recommendation, or favoring by the United States government or Lawrence Livermore National Security, LLC. The views and opinions of authors expressed herein do not necessarily state or reflect those of the United States government or Lawrence Livermore National Security, LLC, and shall not be used for advertising or product endorsement purposes.

# **Evaporation and Propagation of Liquid Drop Streams at Vacuum Pressures, Experiments and Modeling**

Daniel R. Guildenbecher<sup>a,\*</sup>, John J. Barnard<sup>b</sup>, Thomas W. Grasser<sup>a</sup>, Anthony M. McMaster<sup>a</sup> Robert B. Campbell<sup>a</sup>, David P. Grote<sup>b</sup>, Prabal Nandy<sup>a</sup>, and Max Light<sup>c</sup>

<sup>a</sup>Sandia National Laboratories, Albuquerque, NM, USA
 <sup>b</sup>Lawrence Livermore National Laboratories, Livermore, CA, USA
 <sup>c</sup>Los Alamos, National Laboratory, Los Alamos, NM, USA

Accepted for Publication in *Physical Review E*, March 19, 2021

#### **Abstract**

Evaporation of streams of liquid droplets in environments at vacuum pressures below the vapor pressure has not been widely studied. Here, experiments and simulations are reported that quantify the change in droplet diameter when a steady stream of  $\approx 100~\mu m$  diameter drops is injected into a chamber initially evacuated to  $< 10^{-8}$  bar. In experiments, droplets fall through the center of a 0.8 m long liquid nitrogen cooled shroud, simulating infinity radiation and vapor mass flux boundary conditions. Experimentally measured changes in drop diameters vary from  $\approx 0$  to 6  $\mu m$  when the initial vapor pressure is increased from  $10^{-6}$  to  $10^{-3}$  bar by heating the liquid. Measured diameter changes are predicted by a model based on the Hertz-Knudsen equation. One uncertainty in the calculation is the "sticking coefficient",  $\beta$ . Assuming a constant  $\beta$  for all conditions studied here, predicted diameter changes best match measurements with  $\beta \approx 0.3$ . This value falls within the range of  $\beta$  reported in the literature for organic liquids. Finally, at the higher vapor pressures conditions considered here, the drop stream disperses transverse to the main flow direction. This spread is attributed to forces imparted by an absolute pressure gradient produced by the evaporating stream.

#### Introduction

Injection of liquid droplet streams into environments at vacuum or near vacuum conditions has been proposed for several applications. Muntz and Orme [1] review the associated technical challenges and summarize a number of applications. Since then, progress has continued in the science and application of liquids in vacuums. Examples in the recent literature include thermal radiators [2], momentum exchange for tandem spacecraft positioning [3,4], and liquid thrusters [5]. These and many other applications require a fundamental ability to predict and control the propagation and evaporation of low to moderate vapor pressure liquids into an ambient environment at pressures significantly below the vapor pressure.

Likely due to the experimental challenges, the literature contains limited measurements of the evaporation and propagation of liquid droplets into vacuum environments. Muntz and Dixon [6] provide a motivating example. In that work, streams of liquid droplets with diameter on the order of a few hundred μm were injected into the top of a vacuum facility initially evacuated to 10<sup>-8</sup> bar. Two liquids were considered with vapor pressures between 10<sup>-7</sup> to 10<sup>-11</sup> bar. As discuss in Muntz and Dixon [6] and expanded upon in Muntz and Orme [1], experimental measurements focused on the formation and propagation of the droplet stream. Results demonstrated very small stream dispersion after falling through a 5.5 m long vacuum flight tube. This led Muntz and Orme [1] to conclude that similar droplet streams in space could be made to propagate many kilometers with good control. Subsequently, these and other authors have used similar methods to study the collision of two droplet streams under vacuum

<sup>\*</sup> Corresponding author: drguild@sandia.gov

conditions [7,8]. Additional work motivated by droplet radiator applications has also been reported by NASA [9] and even conducted on Russia's Mir space station [10].

These investigations primarily consider liquids of very low vapor pressure (10<sup>-7</sup> bar or less). Within the practical confines of experimental facilities, mass loss due to evaporative cooling is typically insignificant. Still, in space applications it may be necessary to propagate droplet streams over such long distances that mass loss is of concern. Furthermore, other applications may benefit from or necessitate the use of higher-vapor pressure fluids. Motivated by waste disposal in space, some limited experimental studies of the flash-boiling of extremely high vapor pressure fluids, such as water, have been conducted [11]. However, there appears to be a paucity of data on the evaporation of moderate vapor pressure fluids, which are unlikely to flash-boil but may nevertheless display measurable evaporation within practical experimental confines.

Motivated by this, the current work discusses new experiments and modeling of the propagation and evaporation of droplet streams of varying vapor pressures into vacuum environments. The work begins with a discussion of the experimental facility, data processing methods, and results. Following this, modeling is presented and validated against the measured changes in droplet diameters. In addition, a self-dispersal of the evaporating droplet stream is experimentally observed and hypothesized to originate from the pressure gradient established by the evaporated vapor. Finally, the work concludes with a summary of the findings and recommendations for future investigations.

# **Experimental Methods**

Materials

The experimental test liquid is DowTherm  $Q^{TM}$ , which is an industrial heat transfer fluid with a molecular mass of 190 g/mol. Figure 1 plots the vapor pressure,  $p_{vap}$ , as a function of liquid temperature,  $T_l$ , as reported by the manufacturer data sheets [12,13]. For this liquid, vapor pressure varies by many orders of magnitude between approximately room temperature (300 K) and a few hundred degrees above room temperature. These temperatures are experimentally feasible; therefore, this liquid was selected to enable experimental conditions spanning a wide range of initial rates of evaporation.

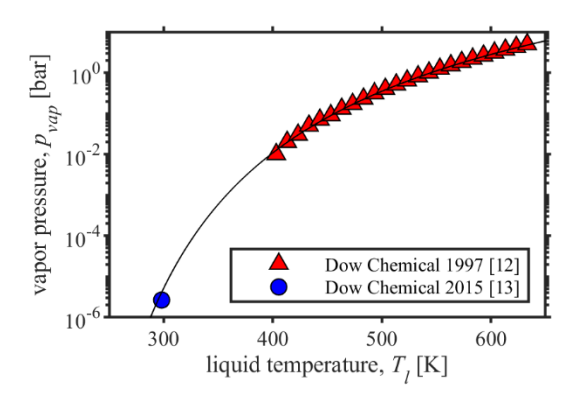


**Figure 1.** Vapor pressure of DowTherm Q<sup>TM</sup>

To facilitate modeling, the vapor pressures reported by the manufacturer (symbols in Figure 1) are parameterized by the best-fit cure shown by the black line and given by

$$p_{vap} = 1.339 \times 10^{-9} \cdot T_l^{2.83} \cdot e^{8.71 - 2371.6/(T_l - 157)} \text{ [bar]}.$$
 (1)

Similarly, other relevant properties of DowTerm Q<sup>TM</sup> [12,13] are parameterized as

$$\rho_l = 1.1877 - 0.0007576T_l [g/cm^3], \tag{2}$$

$$c_{yl} = 22.8518(0.766 + 0.003035T_l)$$
, and (3)

$$L = 0.7483 - 6.02578 \times 10^{-7} T_I^2 - 3.2492 \times 10^{-10} T_I^3 \text{ [eV]}.$$
 (4)

Here,  $\rho_l$  is the density,  $c_{vl}$  is the specific heat at constant volume, and L is the latent heat of vaporization. In Eq. (1)-(4)  $T_l$  is in units of Kelvins. Note, Eq. (3) and the rest of this work uses the dimensionless form of  $c_{vl} = (1/k_b) \cdot de_l/dT_l$  where  $e_l$  is the internal energy per molecule, and  $k_b$  is the Boltzmann constant. Eq. (3) is found by curve-fitting the dimensional specific heat values given in [12,13] and dividing by the ratio of  $k_b$  to the molecular mass. For the range of conditions of interest to the current study, the dimensionless value of  $c_{vl}$  is on the order of 40. This is much higher than the theoretical value of 3/2 for a perfect monatomic gas but is typical of complex organic molecules, such as DowTherm  $Q^{TM}$ , with many internal degrees of freedom.

# Experimental Configuration

The experimental configuration is motivated by the pioneering work of Muntz and Dixon [6]. Figure 2 shows a schematic of the facility with photos in Figure 3. A 2.5 m tall and 44.5 cm inner diameter cylindrical vacuum chamber is evacuated to an ultimate pressure ≤10<sup>-8</sup> bar. Liquid is syringe pumped at ml/hr volumetric flow rates through a degassing chamber to reduce dissolved gases and then into a droplet generator. The droplet generator utilizes a piezo to excite the breakup of the liquid jet resulting in a stream of nearly mono-disperse droplets. The injection nozzle is heated to vary the initial droplet temperature. As the droplets fall through the vacuum chamber, evaporation creates a vapor phase. This is trapped using an annular shroud filled with liquid nitrogen (LN2). Finally, droplet evaporation is quantified by measuring the droplet diameters both upstream and downstream using high-speed cameras coupled to long working-distance microscopes. In the paragraphs that follow, system components are discussed in detail.

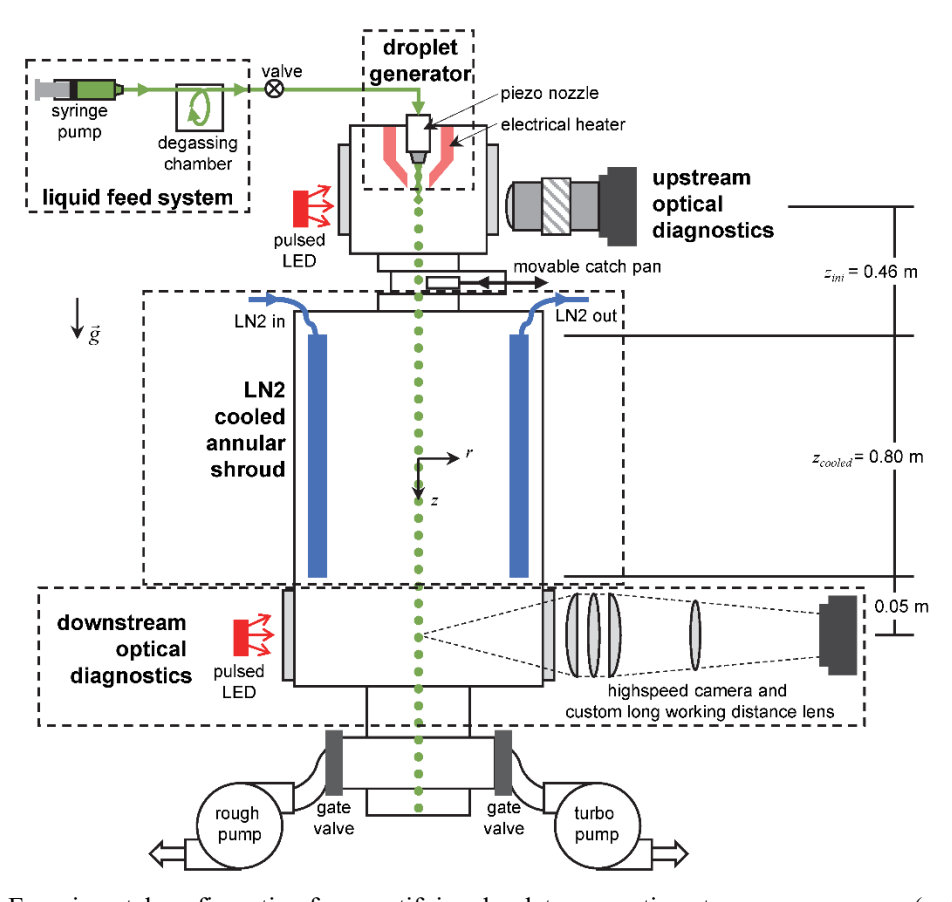


Figure 2. Experimental configuration for quantifying droplet evaporation at vacuum pressures (not to scale)

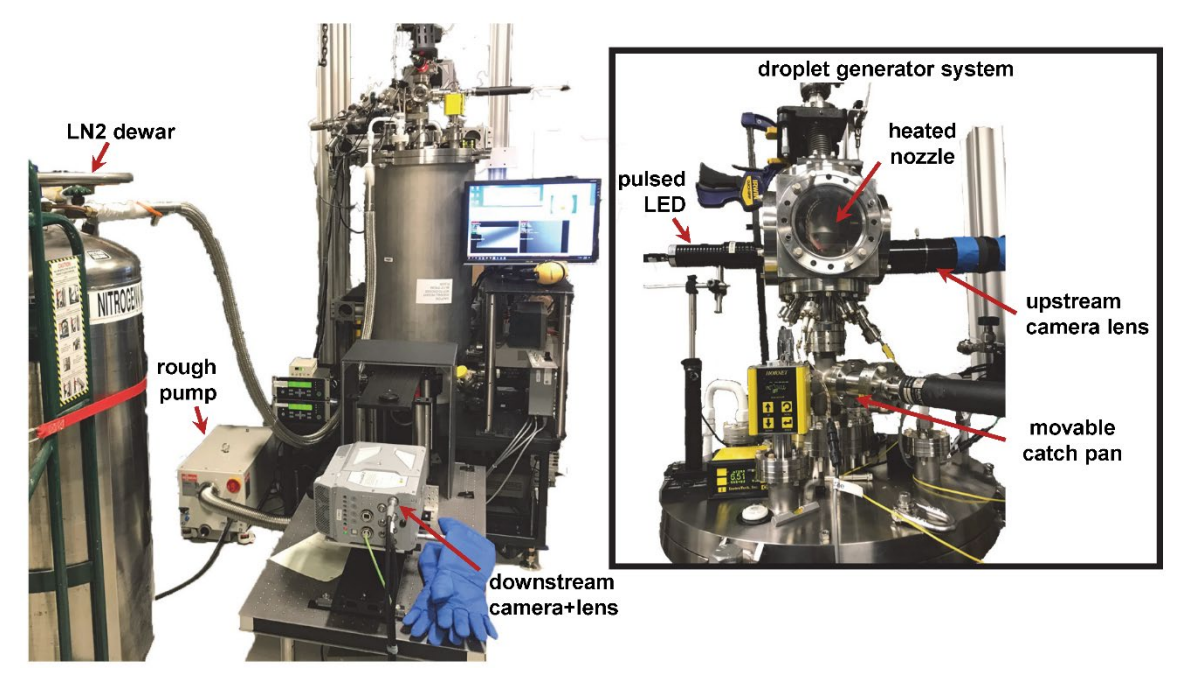


Figure 3. Experimental configuration as assembled in the laboratory

The vacuum chamber is a custom designed, modular system based on a typical "bell-jar" configuration. In an experiment, the chamber is first evacuated using a scroll pump (Bush Cobra BA 0100 C). Once pressure is

reduced close to the pump's ultimate limit (~10<sup>-5</sup> bar), a gate valve connected to the rough pump is closed and a second gate valve connected to a turbo pump (Leybold Turbolab) is opened. Vacuum pressures are monitored using two Convectron® gauges placed at the top and bottom of the chamber. These are generally accurate from atmospheric to ~10<sup>-7</sup> bar. In addition, an ion gauge (InstruTech Hornet IG4YF) is installed at the top of the chamber. This is generally accurate from ~10<sup>-6</sup> to as low as 10<sup>-13</sup> bar. Initial measured pressures are in the range of 10<sup>-8</sup> to 10<sup>-9</sup> bar as indicated by the ion gauge. It should be noted these gauges are operated using their factory calibrations based on air or nitrogen. In the experiments reported here, the chamber is initially filled with air during the pump-down and prior to liquid injection. Following liquid injection, evaporation leads to a gas-phase environment, which is a mixture of remaining air plus vaporized DowTherm Q<sup>TM</sup>. At that point, the pressure gauge calibrations are likely invalid.

Several technologies are commercially available to produce a stream of droplets [14]. Here, a piezo droplet generator is selected due to previous application for droplet injection into vacuum [6-9,15] and evaporation studies at atmospheric pressure [16]. In the current work, piezo nozzles are supplied by MicroFab Technologies Inc. of Plano, Texas. In this design, liquid first passes through a small glass tube, surrounded by a co-axial piezo. Liquid then exits through a contoured µm-sized glass tip to produce a laminar jet. In an experiment, the piezo is driven by a square wave (produced by Tektronix model AFG 3022B function generator and ThorLabs model HVA200 20× voltage amplifier) at a frequency close to the to the capillary instability frequency [17]. When necessary, the frequency and voltage are adjusted while viewing live images from the optical imaging to produce a continuous, steady stream of nearly monodisperse droplets.

Initial liquid temperature is controlled using a MicroFab Technologies nozzle heater, originally designed for printing of molten solder up to 250 °C. Electrical heaters are embedded into aluminum blocks that surround the nozzle and a stainless-steel pre-filter. Thermocouples, also embedded in the aluminum blocks, are used for active feedback. This radiatively heats the nozzle tip and filter. Without convective heat losses and assuming minimal conductive heat losses through the  $\approx 3$  mm stainless-steel feed-tube, the steady state temperature of the nozzle and the liquid within equals the temperature of the surrounding heater.

The insert in Figure 3 shows a photo of the droplet generator as physically installed at the top of the vacuum chamber. Wires for the piezo driver, electrical heater, and thermocouple are run through Ultra High Vacuum (UHV) ports located on the side and bottom of the optically accessible cube. During startup and shutdown of the droplet injection, the liquid stream can be unstable with periodic dribbling and sputtering caused by transient flow rates. To reduce potential contamination of the main vacuum chamber during these transients, a custom machined orifice plate with a  $\approx 15$  mm diameter through hole is located immediately below the cube. The underside of this orifice plate includes an annular groove intended to reduce wicking of the liquid to the outer walls. A catch pan is located below this orifice plate and is attached to a UHV sealed translation stage. In experiments, the catch pan is translated away from the stream allowing the droplets to enter the main chamber only after a stable stream is verified in live images from the upstream camera system discussed in the next subsection. Finally, to maintain alignment of the droplet stream within the centerline of the vacuum chamber, the piezo nozzle and heater assembly

are mounted on a tip-tilt stage as shown in the insert in Figure 3. This allows real-time adjustment of the physical pointing of the nozzle assembly when operating under vacuum.

Liquid is fed into the nozzle through a syringe pump that typically achieves constant volumetric flow rate by pushing on a syringe plunger at fixed velocity. With a downstream pressure of approximately zero and relatively small pressure drop across the nozzle, the feed pressure is well below atmospheric. To prevent the liquid from being sucked into the chamber at a flow rate faster than the pump speed, the syringe plunger is clamped onto the pump.

During initial testing of droplet injection into vacuum, some random in-flight shattering of droplets was observed. Based on literature suggestions [7], droplet shattering was attributed to vapor release from dissolved gasses within the liquid. This is addressed by first pumping the liquid through a ~200 mm length of gas-permeable tubing (0.6 mm ID Teflon AF® tubing supplied by Biogeneral Inc of San Diego, California) installed in a separate vacuum chamber. As liquid passes through the tube, the external vacuum draws the dissolved gasses through the gas-permeable tubing. When using this degassing method, no further random droplet shattering is observed for the experiments reported here.

Finally, as the droplets fall through the vacuum chamber, evaporation releases vapor into the chamber. This vapor is trapped with a liquid nitrogen (LN2) cooled annular shroud as illustrated in Figure 2. Vapor molecules are assumed to freeze onto the shroud, which is at LN2 temperatures (-196 °C) and is well below the reported freezing point of DowTherm Q<sup>TM</sup> (<-26 °C given in Dow Chemical [13]).

#### Experimental Diagnostics

High-magnification, backlit imaging is commonly applied for measuring droplet properties [18]. Where the optical standoff is small, commercial lenses and cameras can achieve videos with magnified pixel sizes on the order of µm and record rates of many thousands of frames-per-second. Droplet sizes and velocities can be quantified by any number of image-processing routines, including methods previously developed by the authors [19-23]. In addition, these cameras provide the ability to visualize the droplet stream in real-time. This is particularly advantageous for the current application where real-time adjustment of experimental settings is needed to maximize the stability of the droplet stream. For these reasons, high-magnification, high-speed imaging was selected as the primary droplet diagnostic.

At the upstream location show in the insert in Figure 3, the standoff distance between the droplet stream and the exterior of the optical windows is relatively small ( $\approx 10$  cm). At this standoff, a commercial high-magnification lens (Infinity K2 Long Distance Microscope) and high-speed camera (Photron SA-Z) provides sufficient magnification. To freeze droplet motion, the field of view is backlit with a pulsed red LED (HPLS-36 from Lightspeed Technologies, Inc.) synchronized to the camera, providing frame illumination times on the order of a few hundred ns.

Over the 1.31 m fall-height between the upstream and downstream fields of view, small deviations in the initial pointing of the droplet stream cause substantial variation in the downstream radial position. It is assumed that direct impact of the droplet stream onto the walls of the UHV chamber would cause significant contamination of the vessel that might be impossible to clean. Therefore, to minimize contamination, the downstream optically accessible

vacuum section maintains the 44.5 cm internal diameter of the main vacuum chamber. The addition of optical windows results in a standoff distance between the centerline and the window exterior of ~30 cm. This exceeds the standoff distance possible with the commercial lens utilized at the upstream position. Instead, downstream imaging is achieved with the custom long-working distance lens system developed in Guildenbecher *et al.* [24]. Once again, video images are recorded with a high-speed camera (Photron SA-Z) backlit with a pulsed red LED (HPLS-36 from Lightspeed Technologies, Inc.).

Prior to an experiment, optical magnification is quantified by imaging a metrology grade dot grid with known dot diameters and spacing (Max Levy Autograph DA020 with NIST traceable dimensions given to within  $\pm 0.9~\mu m$ ). These images are processed using the circular Hough transform in MATLAB® to locate the dot centers. For the downstream configuration the measured effective pixel size,  $\Delta x = 6.26 \pm 0.04~\mu m$ , defined as the mean  $\pm$  the standard deviation across the field of view. To verify this result is not affected by window distortions due to vacuum, calibration is performed at both atmospheric and vacuum conditions, resulting in less than 0.02% difference in the mean effective pixel size. Because the main quantity of interest is the change in droplet diameter between the upstream and downstream locations, the effective pixel size of the upstream camera system,  $\Delta x = 6.25 \pm 0.04~\mu m$ , is closely matched to the downstream configuration. This ensures that diameter measurement biases, which are a function of pixel size, are similar in the upstream and downstream fields-of-view and are therefore removed when the results are subtracted to find the change in diameter.

Figure 4 shows select frames from experimental videos recorded when the droplet generator is at room temperature (24°C as measured by the thermocouple within the heater block). Both the upstream and downstream videos are recorded at 100000 frames per second (280×640 pixel resolution) with 12779 total frames per video. Background intensity variations are first removed by fitting a rotated two-dimensional Gaussian function to the average image intensity and then normalizing each image by this function. Next, the dark droplets are segmented from the light background using the methods discussed in Guildenbecher *et al.* [22]. For every droplet, an optimum segmentation threshold is determined from the grayscale threshold value that maximizes the image sharpness (quantified by the magnitude of the Sobel gradients) along the identified droplet edges. Following this, the trajectories of individual droplets are determined using the methods defined in Guildenbecher *et al.* [20]. Briefly, droplet trajectories are found by matching measured regions to their nearest neighbor in the subsequent frame. The process is repeated until each droplet is measured as a single trajectory that originates at the top of the field of view and ends at the bottom of the field of view.

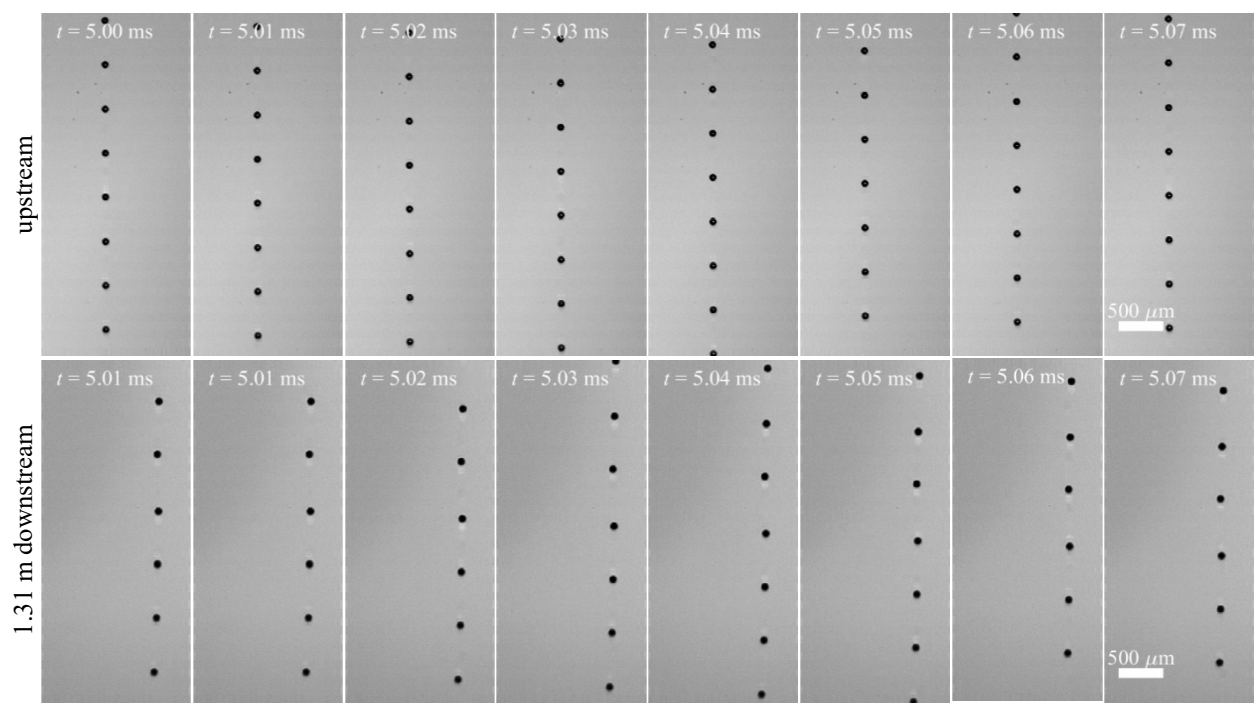


Figure 4. Select experimental video frames when the nozzle is at room temperature (24°C).

Figure 5 shows example results when the videos in Figure 4 are processed in this manner. Here, measured droplet outlines are colored by the mean area equivalent diameter,

$$d = \Delta x \cdot \sqrt{4N_{pixels}/\pi} \ . \tag{5}$$

where  $N_{pixels}$  is the total number of pixels within each segmented region, and the overbar indicates averaging over all measured frames within the trajectory. To reduce the effect of measurement outliers, the mean in Eq. (5) is found by fitting the measured diameters as a function of time to a constant with a robust, bisquare weight function and tuning coefficient of 2 in MATLAB®. Similarly, arrows in Figure 5 show the measured droplet velocities, with a 10 m/s reference arrow shown on the bottom-right. Velocities are determined by fitting the horizontal and vertical positions as a function of time to a line, again using robust fitting to reduce the effects of outliers. Note, this data processing provides a robust measure of individual *mean* droplet diameters and velocities *within* the field of view of each camera. Changes in drop diameters and velocities over the 4.0 mm vertical extent of each field of view are negligible compared to differences expected over the 1.31 m fall height between the upstream and downstream cameras.

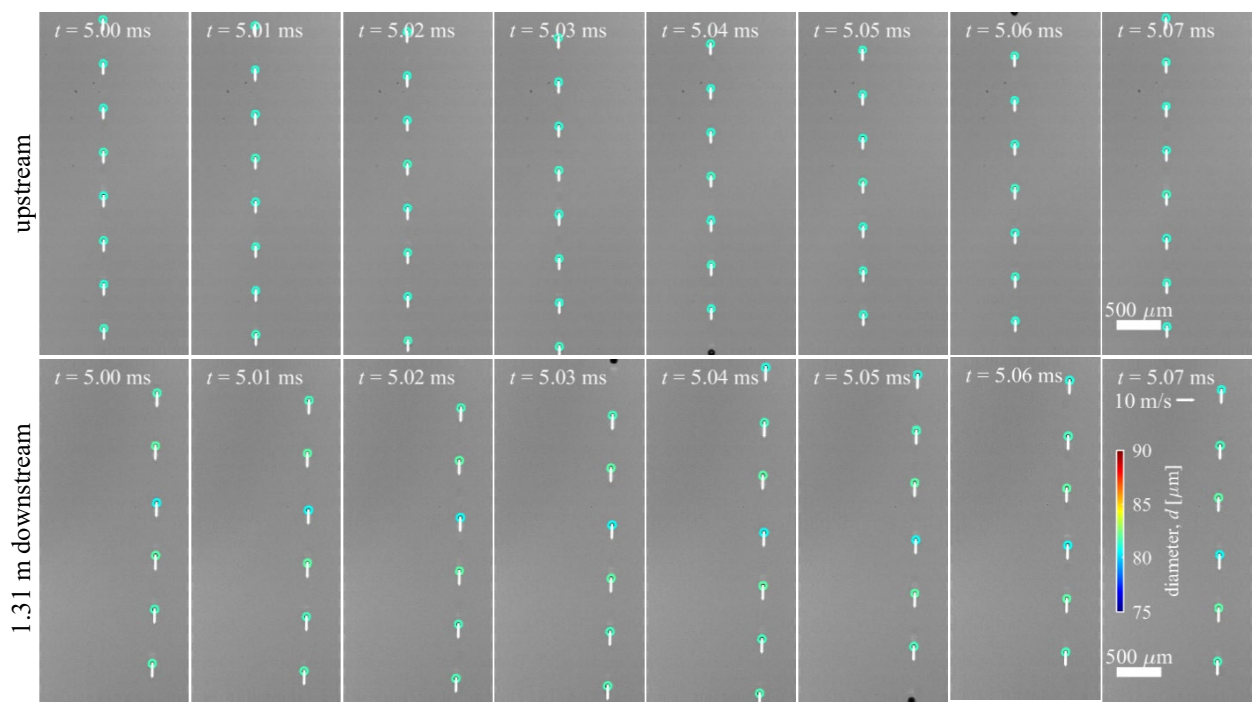


Figure 5. Select experimental results with the nozzle at room temperature (24°C).

For the example in Figure 5, 1764 and 1763 total drops are measured upstream and downstream, respectively. Accounting for the total record time, the measured droplet frequency is 13.80 and 13.80 kHz, upstream and downstream respectively. This closely matches the applied piezo frequency of 13.76 kHz, indicating that both fields of view quantify essentially all expected drops. Vertical velocities are 7.073±0.001 m/s at the upstream location, reported as the mean ± standard deviation. At the downstream location, vertical velocities are 8.712±0.003 m/s. Accounting for the local latitude and altitude in Albuquerque, New Mexico [25], acceleration due to gravity, *g*, is 9.792 m/s². Assuming the droplets fall in vacuum without drag, the measured initial and final velocities are used to quantify the droplet residence time between the measurement locations, 0.167s, as well as the total fall height, 1.320 m. This matches the physical distance between the upstream and downstream diagnostics of 1.306±0.005 m to within 2%.

The accuracy of droplet diameter measurements is likely a function of the optical configuration and the image processing routines used to extract the droplet edges. To quantify and remove potential biases, a dot grid with dot diameters ranging from 63 to 1000  $\mu$ m (Max Levy Autograph DA020 with NIST traceable dimensions given to within  $\pm 0.9~\mu$ m) is placed within the image focal plane in the vacuum chamber. Image sets are recorded both upstream and downstream to capture each dot diameter within the grid. These data are processed identically to the droplet data described above, with the exception that no temporal tracking is necessary. Results are used to find a correction between the raw measured diameters and the true diameters. For the range of values considered here, diameter corrections are found to be sub-pixel in magnitude ( $\sim 1-4~\mu$ m). All droplet diameters reported in this work have been corrected in this manner.

Finally, the accuracy of diameter measurements is also adversely affected if individual droplets fall outside of the relatively narrow depth of field of the high-magnification imaging optics. Here, droplet sharpness is

determined from the mean of the magnitude of the normalized image Sobel gradients for all pixels immediately inside and outside of the measured droplet perimeters. Based on visual inspection of the raw data, any droplet with mean sharpness less than or equal to 4.0 is considered out-of-focus and removed from the final droplet statistics. Note, for the example shown in Figure 5, none of the 1764 measured upstream droplets and only 62 of the 1763 measured downstream droplets (3.5%) are found to be out-of-focus.

After applying the data processing techniques discussed above, the measured diameters for the example shown in Figure 5 are  $81.2\pm0.1~\mu m$  and  $81.5\pm0.3~\mu m$  upstream and downstream, respectively. Again, values are given as the mean  $\pm$  standard deviation. Assuming Gaussian statistics, the precision of the mean is given by

$$\pm k\sigma/\sqrt{N}$$
, (6)

where  $\sigma$  is the standard deviation, N is the number of measurements, and k is a constant that depends on N and the desired confidence bounds. For large values of N, as considered here, the 99% confidence bound is determined by k = 2.58. From Eq. (6) the 99% confidence in the mean measured diameters is  $\leq 10^{-2} \, \mu m$ , indicating that measurements have acquired enough data to be statistically converged.

Finally, for the current example, the measured change in mean drop diameter is  $\pm 0.3$  µm. At the low initial temperature in this example (25°C), the vapor pressure is around  $3\times10^{-6}$  bar (Figure 1) and modeling, discussed in a subsequent section, predicts essentially zero diameter change. It is therefore assumed that the slight positive change in diameter is a measure of remaining measurement biases, equivalent to  $\sim 1/20$  of the effective pixel size and 0.3% relative uncertainty with respect to the mean diameter.

#### **Experimental Results**

Figure 5 shows typical experimental results recorded when the nozzle is at room temperature. Similarly, Figure 6 shows typical experimental results with the heater at a 40°C setpoint. To allow the nozzle and liquid within to achieve thermal equilibrium, for all heated nozzle experiments a minimum 15-minute thermal-soak time is implemented between the instant the thermocouple embedded in the heated aluminum block reaches its setpoint and recording of experimental results. During this period, the droplet stream is continuously monitored with the upstream and downstream diagnostics. The driving piezo frequency and voltage are adjusted as necessary to maintain a monodisperse droplet stream. In addition, the pointing of the stream is adjusted using the tip-tilt stage to keep the droplets well-centered within the focus of the downstream diagnostics. Finally, at the end of the thermal-soak time, video data are recorded.

Interestingly, as seen in Figure 6, at a 40°C initial temperature, the droplet stream has spread in the horizontal direction at the downstream location with the spatial offset appearing to follow a periodic sinusoid. Nevertheless, essentially all expected droplets are measured within the downstream field of view as indicated by the close agreement between the measured droplet frequency (13.70 kHz) and the applied piezo frequency (13.66 kHz).

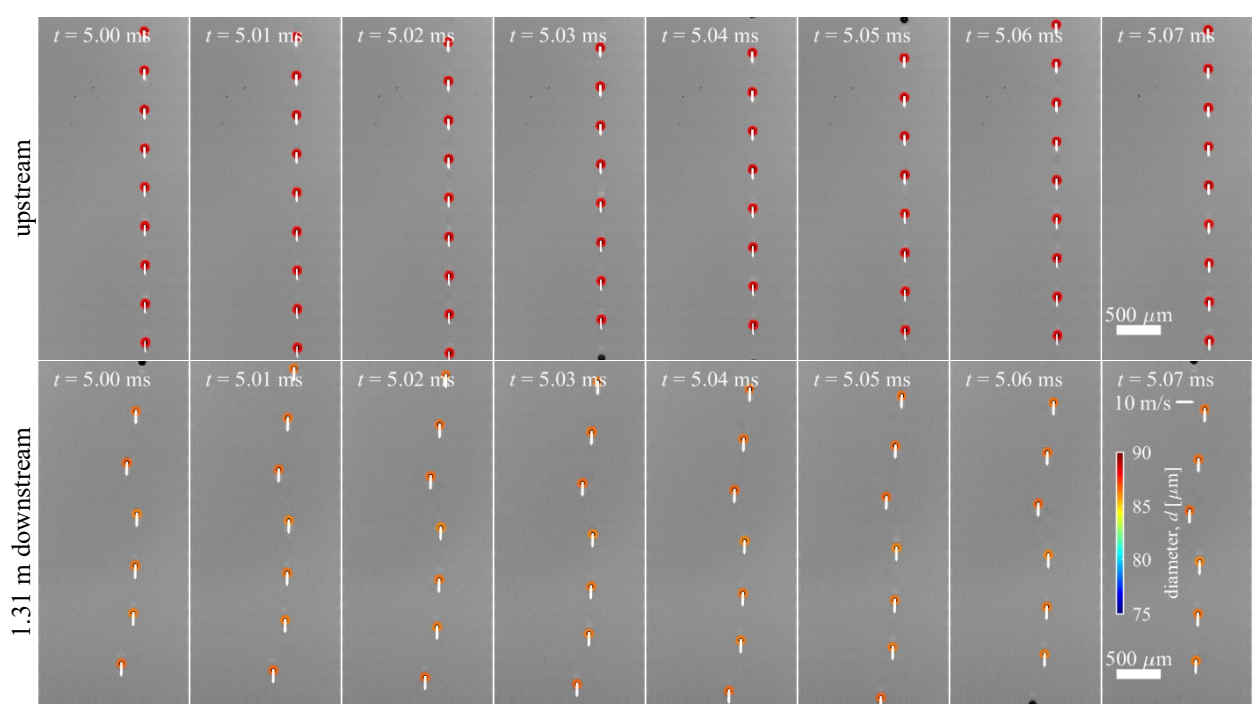
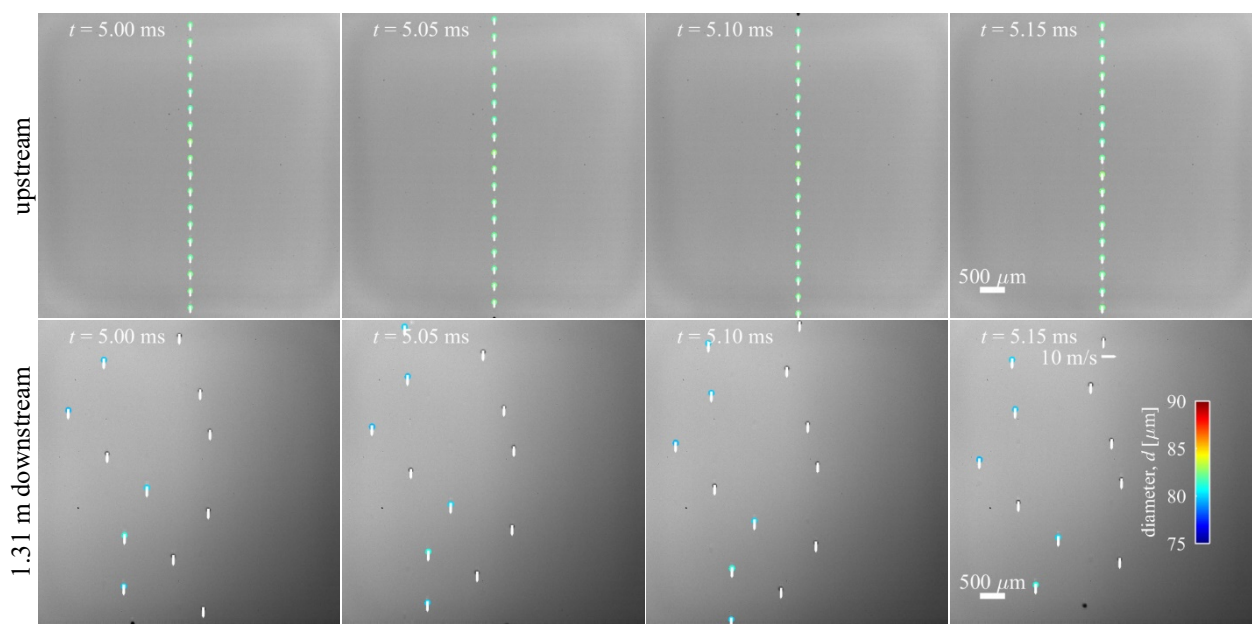


Figure 6. Example experimental results with the nozzle at 40°C.

Next, Figure 7 shows typical results when the temperature setpoint is increased to 60°C. As seen in Figure 7, the downstream spread in the droplets increases significantly at this condition. Consequently, to capture the entirety of the droplet spread, the downstream field of view is expanded compared to the measurements discussed thus far. This is achieved by reducing the record rate to 20000 frames per second. At this frame rate, the camera records data at all pixels in the sensor array (1024×1024 pixels). Note that the optical configuration has not changed from Figure 6 to Figure 7, and the effective pixel size remains the same as reported above. With this increased field of view, all expected droplets are still measured within the downstream field of view as indicated by the close agreement between the measured droplet frequency (13.30 kHz) and the applied piezo frequency (13.39 kHz). However, 40% of the measured drops at the downstream position are found to be out-of-focus as quantified by the edge sharpness criteria. In Figure 7 these out-of-focus drops are indicated by velocity vectors without diameter outlines.



**Figure 7.** Example experimental results with the nozzle at 60°C.

Finally, Figure 8 shows typical results when the temperature setpoint is increased further to 80°C. At this condition, the droplet stream expands further in the downstream field of view. Although the measured droplet frequency (13.57 kHz) still closely matches the applied frequency (13.62 kHz), a large majority (91%) are found to be out-of-focus and not included in diameter statistics.

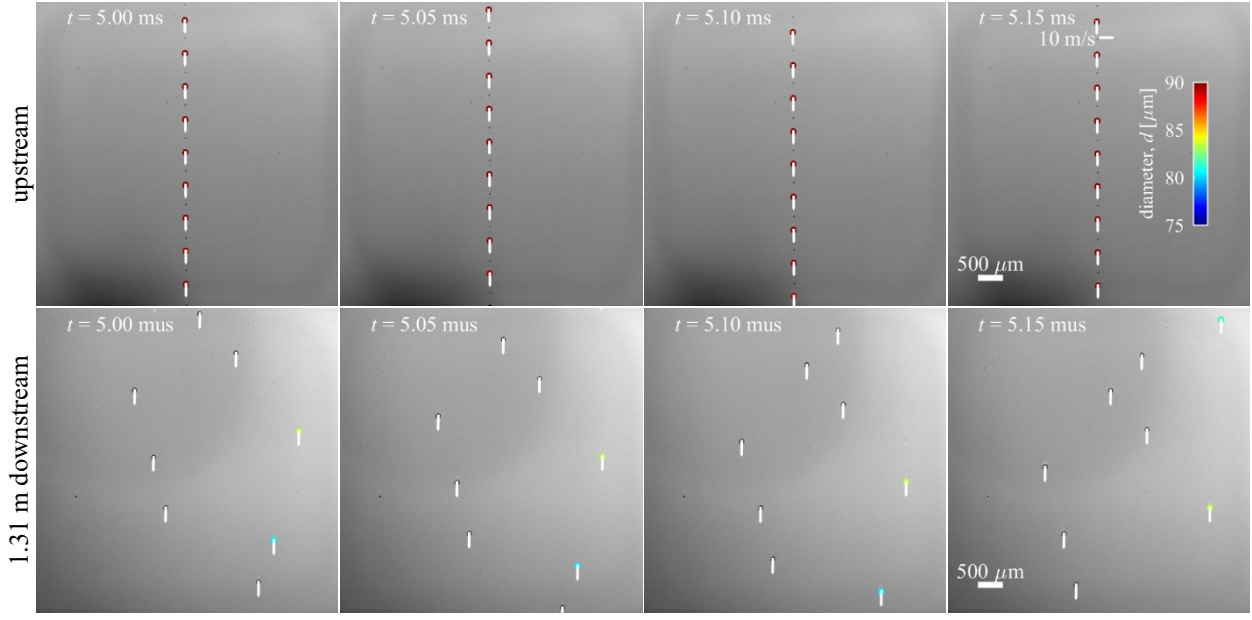


**Figure 8.** Example experimental results with the nozzle at 80°C.

As discussed in detail in the next section, the spread of the droplet stream in the horizontal direction is believed to be caused by pressure gradients that cannot be mitigated in the current experimental configuration. Because a large percentage of the droplets spread outside of the downstream depth of field, measurements conducted at initial temperatures greater than  $\sim 80$  to 100 °C have not been successful.

In total, four experimental runs were conducted on four separate days spanning slightly more than a month. Table 1 summarizes the measured drop statistics. Video results for each recording are processed as described above. Measured drop frequencies are generally in close agreement with the applied piezo frequencies shown in the third column. The exception being at the downstream location for temperatures ≥80°C where measured frequencies are significantly less than the applied frequency because the horizontal extent of the droplet stream has spread beyond the field of view.

In Table 1, measured droplet velocities and diameters are reported as the mean  $\pm$  standard deviation. Diameter statistics are determined from only in-focus drops with sharpness  $\geq$  4. Note that a few upstream measurements are found to be slightly out-of-focus such that no diameters are quantified. In addition, for measurements at elevated initial temperatures, the total number of in-focus drops at the downstream field of view is signifyingly lower than upstream due to many drops being out-of-focus.

Finally, and perhaps most importantly, the measured change in diameter is defined as the mean diameter measured downstream minus upstream and is given in the final column of Table 1. Figure 9 plots the measured changes in diameters versus the initial nozzle temperature. Here, error bars show the 99% confidence interval determined as the sum squared of the confidence in mean upstream and downstream diameters as given by Eq. (6). To highlight trends, the solid line in Figure 9 shows the best-fit line which relates average change in diameter as a function of temperature. Curve fitting is performed with the MATLAB® curve fitting toolbox. To account for the precision of each measurement, data in Figure 9 is weighted by the number of in-focus drops used to determine each data point, as given in Table 1. The dashed lines show the 99% confidence bounds for the best-fit as reported by MATLAB®.

Despite scatter in the data, the measured trend agrees with the overall expectation of reduced diameters at higher initial temperatures due to enhanced evaporation. As reported in Table 1, other relevant conditions, such as the initial drop diameters and velocities, vary somewhat with recording number. These quantities would also be expected to effect the change in diameter due to evaporation. Therefore, in the modeling discussed in the next section, each experimental data point is predicted by incorporating the measured variation of all upstream quantities reported in Table 1.

 Table 1. Measured evaporation results

	Condition	ns	Upstream Measurements					Downstream Measurements					
	Nozzle	Applied	Drop	Vertical	Horizontal			Drop	Vertical	Horizontal			Change in
Record	Temp	Frequency	Frequency	Velocity	Velocity	Number	Diameter*	Frequency	Velocity	Velocity	Number	Diameter*	Diameter,
Number	[°C]	[kHz]	[kHz]	[m/s]	[m/s]	in Focus	[µm]	[kHz]	[m/s]	[m/s]	in Focus	[µm]	$\Delta d^*$ [µm]
Run 1													
1	50	11.00	11.05	6.559±0.001	-0.006±0.001	1412	116.3±0.2	11.04	8.316±0.003	-0.105±0.002	1410	114.2±0.2	-2.1
Run 2													
1	24	13.03	13.07	$7.739\pm0.002$	$0.019\pm0.001$	1670	$113.3 \pm 0.1$	13.07	$9.250\pm0.006$	$-0.128\pm0.003$	0		
2	41	13.43	13.48	$7.370\pm0.001$	$0.019\pm0.001$	1722	$95.3\pm0.1$	13.47	$8.956\pm0.003$	-0.123±0.002	1721	93.4±0.3	-1.9
3	60	13.53	13.57	$8.485\pm0.001$	$0.007\pm0.002$	1734	$94.2 \pm 0.1$	13.59	$9.897 \pm 0.006$	$-0.121\pm0.002$	1737	92.1±0.3	-2.1
4	80	13.43	13.44	$8.133\pm0.002$	$0.024\pm0.002$	1466	$89.8 \pm 0.2$	12.93	$9.609\pm0.024$	$-0.134\pm0.009$	506	$85.4 \pm 0.6$	-4.3
5	80	13.62	13.63	$9.418\pm0.002$	$0.039\pm0.002$	1486	$89.9 \pm 0.5$	13.57	$10.760\pm0.008$	-0.161±0.018	128	82.3±1.5	-7.6
6	100	13.81	13.81	$10.545 \pm 0.004$	$0.048\pm0.002$	1506	92.3±0.8	12.99	$11.733\pm0.010$	$-0.213\pm0.035$	193	88.4±1.0	-3.9
7	100	13.64	13.70	$5.281\pm0.001$	$-0.017 \pm 0.002$	0		2.70	$7.370\pm0.038$	$-0.106\pm0.012$	18	87.9±1.5	
Run 3													
1	24	13.50	13.58	5.277±0.001	$0.001\pm0.001$	1735	87.8±0.1	13.55	$7.320\pm0.003$	-0.093±0.002	1		
2	24	13.40	13.46	$6.518\pm0.001$	$0.006\pm0.001$	1720	$87.5\pm0.1$	13.43	$8.278\pm0.003$	$-0.112\pm0.002$	544	$86.6 \pm 0.3$	-0.9
3	41	13.40	13.47	$6.046\pm0.001$	$0.005\pm0.002$	1721	$78.8 \pm 0.5$	13.43	$7.890\pm0.004$	$-0.094\pm0.003$	55	$74.5 \pm 0.3$	-4.3
4	60	13.39	13.48	$4.667 \pm 0.001$	$0.001\pm0.001$	1470	82.1±0.2	13.30	$6.933 \pm 0.011$	$-0.092\pm0.011$	874	$78.8 \pm 1.1$	-3.3
5	60	13.39	13.48	$4.664\pm0.001$	$0.001\pm0.001$	1470	82.1±0.2	12.65	6.923±0.014	$-0.099\pm0.022$	206	$70.0 \pm 1.1$	-4.1
Run 4													
1	24	13.76	13.80	$7.073\pm0.001$	$0.019\pm0.001$	1764	81.2±0.1	13.80	8.712±0.003	-0.126±0.002	1701	81.5±0.3	0.3
2	40	13.66	13.72	$6.179\pm0.001$	$0.026\pm0.001$	1753	$88.1 \pm 0.1$	13.70	$7.992\pm0.003$	$-0.115\pm0.003$	1750	$86.6 \pm 0.2$	-1.5
3	40	13.64	13.71	$6.101\pm0.001$	$0.027\pm0.001$	1752	$87.6 \pm 0.2$	13.68	$7.936\pm0.003$	-0.122±0.003	1748	$87.0\pm0.2$	-0.6
4	60	13.59	13.64	$6.834 \pm 0.002$	$0.023\pm0.001$	1482	$84.1 \pm 0.4$	13.59	$8.490\pm0.012$	$-0.166\pm0.019$	0		
5	60	13.53	13.59	$5.648 \pm 0.001$	$0.030\pm0.001$	1474	82.5±0.5	8.41	$7.593\pm0.014$	$-0.120\pm0.022$	0		
6	80	13.43	13.49	$5.909\pm0.002$	$0.068\pm0.001$	0		5.43	$7.870\pm0.014$	$-0.128\pm0.018$	16	74.7±1.1	
7	80	13.43	13.48	$6.014\pm0.002$	$0.087 \pm 0.002$	1469	$80.9 \pm 0.4$	1.36	$7.924\pm0.012$	-0.092±0.019	69	$74.3 \pm 2.2$	-6.6

<sup>\*</sup> Quantified from in-focus drops only. All other data quantified from all tracked drops.

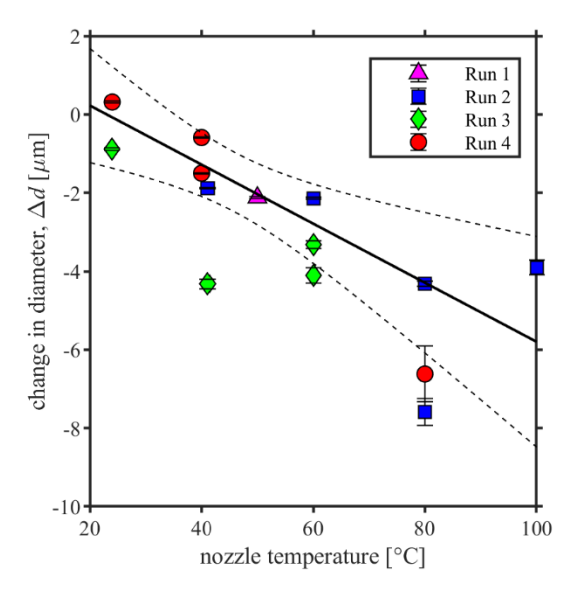


Figure 9. Measured change in diameter as a function of nozzle temperature.

The cause of the data scatter shown in Figure 9 is not completely understood. As mentioned, differences in the initial diameter and velocity likely have some effect. However, careful study of the data in Table 1 reveals that these variations alone do not explain the trends observed at a given nozzle temperature. This likely indicates some remaining experimental variation, which is not well understood or quantified by the chosen measurements. For example, initial droplet temperatures are assumed to be equal to the temperature reported by a thermocouple in the surrounding heated block. These temperatures are equal if the piezo nozzle and filter are in radiative equilibrium with the surrounding heater. To test this assumption, experiments were performed with various thermal soak times. Run 2 utilized a 15-minute thermal soak; Runs 3 and 4 correspond to a 30-minute thermal soak, and the thermal soak for the single data point in Run 1 was signifyingly longer than 30 minutes. For the results in Figure 9, no clear trend is observed as a function of this thermal soak time, perhaps indicating that radiative equilibrium is achieved for all soak times considered. Still, the number of data points are limited, and imprecisely known droplet temperatures cannot yet be ruled out as a source of measurement scatter. In addition, other sources of experimental variation could include unresolved changes in the vacuum pressure during experiments, effects caused by differences in droplet stream pointing leading to variations in boundary conditions, or remaining measurement biases which have not yet been pinpointed.

Despite the scatter, the results in Figure 9 demonstrate experimental resolution of changes in droplet diameters with uncertainty on the order of a micron. This is achieved at droplet fall heights over  $10000^{\circ}$  the initial diameter and an imaging standoff of over  $3000^{\circ}$  the initial diameter, all within UHV vacuum environment with liquid nitrogen cooled walls. In a scaled sense, this is approximately equivalent to dropping a golf ball from the Empire State building and measuring a 0.5 mm diameter change from a vantage point located a city block away.

## Theory and Discussion

The droplet diameter as a function of time, d(t), is predicted with the Hertz-Knudsen equation [26-28]. This formulation estimates the mass flux evaporating from and condensing onto the droplet, together with an energy flux equation, so that both droplet temperature and diameter are solved self-consistently [29]. Let  $N_l$  be the total number of molecules in the liquid droplet such that

$$d = (6N_1/n_1\pi)^{1/3}. (7)$$

Here  $n_l$  is the liquid number density given by  $n_l = \rho_l/m$ , where m is the mass of a single molecule, and  $\rho_l$  is given by Eq. (2).

Mass conservation implies

$$dN_1/dt = \left[ -\beta \phi_{vap} + \beta \phi_{cond} \right] \pi d^2, \tag{8}$$

where  $\phi_{vap}$  and  $\phi_{cond}$  are the vaporization and condensation fluxes, respectively.  $\beta$  is the "sticking coefficient" i.e. the fraction of gas molecules that reach the droplet from the vapor and are not reflected. In Eq (8),  $\beta$  is approximately constant while  $\phi_{vap}$ ,  $\phi_{cond}$  and d vary with respect to time, t. From Hertz [26], Knudsen [27], and Persad and Ward [28] the fluxes are given by

$$\phi_{vap} = n_{g,equil} \sqrt{k_b T_l / 2\pi m} \tag{9}$$

$$\phi_{cond} = n_g \sqrt{k_b T_g / 2\pi m} \ . \tag{10}$$

Here,  $T_g$  is the gas temperature,  $n_g$  is gas number density, and  $n_{g,equil}$  is the equilibrium density when  $T_g = T_l$ . Note,  $n_{g,equil} = p_{vap}/(k_bT_l)$  with  $p_{vap}$  as a function of  $T_l$  given by Eq. (1).

For the condensation flux, Eq. (10), it is assumed that the density,  $n_g$ , is dominated by the vaporized molecules from the preceding and following droplets. In that case, the local gas density is given by

$$n_{\sigma} = n_{\sigma,equil} \left( \Omega / \pi \right) (v'/v) \,. \tag{11}$$

Here  $\Omega = 2\pi[1-(1-d^2/4a^2)^{1/2}]$  is the solid angle subtended by a droplet with center-to-center inter-droplet spacing of a, and v'/v is the ratio of the fluid velocity at the surface of the preceding or following droplet to its value at the droplet. It can be shown that  $v'/v=1/[1+(1-d^2/4a^2)^{1/2}] \approx 1/2$  for a >> d. (For large a, the velocity distribution is less isotropic so the average velocity is closer to the thermal velocity, whereas for a = d/2, the velocity is isotropic over the hemisphere and can be shown to be one half the thermal velocity). In addition, gas molecules are assumed to be at the liquid temperature such that in Eq. (10)  $T_g = T_I$ .

Assuming constant droplet frequency, f, the inter-droplet spacing is given by  $a = v_d/f$  where  $v_d$  is the vertical droplet velocity. With droplets injected downward and neglecting drag, the vertical velocity is given by  $v_d = v_{d,0}(1+gt/v_{d,0})$ . From this,  $a = v_{d,0}(1+gt/v_{d,0})/f$  with  $v_{d,0}$  and f taken from the upstream measurements in Table 1.

Combining Eq. (8)-(11) results in a final expression for the rate of change of molecules within a liquid droplet

$$dN_{l}/dt = -\beta n_{g,equil} \sqrt{k_{b} T_{l}/2\pi m} \left(1 - \Omega/2\pi\right) \pi d^{2}.$$
(12)

Similarly, conservation of energy can be written

$$dE_{l}/dt = \left[-\beta \left(e_{l} + L\right)\phi_{vap} + \beta \left(e_{g} + L\right)\phi_{cond} + \left(1 - \beta\right)\alpha c_{vl}k_{b}\left(T_{g} - T_{l}\right)\phi_{cond}\right]\pi d^{2},$$
(13)

where  $E_l$  is the total energy of molecules in the liquid droplet. In Eq. (13)  $e_g$  is the average thermal energy per molecule transferred to the liquid at gas temperature  $T_g$ .  $e_l$  is the average thermal energy lost from the liquid to the gas at liquid temperature  $T_l$ . L is the latent heat of vaporization of the liquid, given by Eq. (4).  $\alpha$  is the "thermalization" coefficient, which is sometimes also called the "thermal accommodation coefficient". That is, of those particles that are reflected,  $\alpha$  is the fraction of any excess (or deficit) of gas energy per molecule that is transferred to the liquid. For  $\alpha = 0$ , none of the excess (or deficit) of gas energy is transferred to the liquid, whereas for  $\alpha = 1$ , any excess (or deficit) of gas energy is transferred to the liquid. Here it is assumed that  $\alpha = \frac{1}{2}$ . Because evaporative cooling far surpasses condensation, the thermalization term is very small in the current context.

At equilibrium  $T_g = T_l$ ,  $dN_l/dt = 0$  and  $dE_l/dt = 0$ . If not at equilibrium, for example if  $n_g = 0$ ,  $dN_l/dt < 0$  and  $dE_l/dt < 0$ . Note that the latent heat is added to each molecule as it condenses onto the liquid, and the average energy lost from the liquid is the average energy of the liquid plus the latent heat, as only the more energetic molecules (on average) are lost from the liquid.

In Eq. (13)  $e_l$  and  $e_g$  are given by  $\int_0^{T_l} c_{vl} k_b dT_l$  and  $\int_0^{T_g} c_{vg} k_b dT_g$  respectively.  $c_{vl}$  and  $c_{vg}$  are the liquid phase and gas phase specific heat at constant volume, respectively. It is further assumed that the condensation terms are dominated by molecules that originated at  $T_g = T_l$  from the neighboring droplets and the vapor phase specific heat equals that of the liquid,  $c_{vg} = c_{vl}$ . Combined with Eq. (9)-(11) conservation of energy becomes

$$dE_{l}/dt = -\beta n_{g,equil} \sqrt{k_b T_{l}/2\pi m} \left(e_{l} + L\right) \left(1 - \Omega/2\pi\right) \pi d^{2}. \tag{14}$$

The average energy per liquid particle,  $\varepsilon_l$ , is defined as,

$$\varepsilon_t = E_t / N_t \,. \tag{15}$$

This is related to the liquid specific heat via

$$d\varepsilon_{t}/dT_{t} = k_{b}c_{vt}. \tag{16}$$

An analogous expression for gas specific heat is found by replacing l with g in Eq. (16). Using Eq. (15) and (16), the evolution of the liquid temperature is expressed by

$$dT_l/dt = \left(dE_l/dt - \varepsilon_l dN_l/dt\right)/\left(c_{vl}N_l k_b\right). \tag{17}$$

Equations (12), (14), and (17) along with the material properties given in Eq. (1)-(4) provide a set of coupled first order ordinary differential equations for prediction of the evolution of droplet diameter and temperature. Here, Mathematica's NDSolve is used to find the transient solution. Note that the theory above neglects radiation and surface tension effects. At the temperatures and droplet diameters of interest, these effects are expected to be negligible.

In an experiment, droplets are injected with measured initial vertical velocity,  $v_{z,0}$ , and diameter  $d_0$ , at the upstream location (Table 1). As illustrated by the dimensions shown on the right-hand side of Figure 2, droplets initially fall through a  $z_{ini} = 0.46$  m tall vacuum section where the walls are uncooled. It is assumed that vapor equilibrium is established in this section such that no evaporation occurs in the first 0.46 m. Modeling is therefore initialized at 0.46 m from the upstream measurement where it is assumed that the initial temperature is equal to the

nozzle temperature, the initial diameter equals  $d_0$ , and the initial downward velocity is  $(v_{z,0}^2 + 2z_{\text{mig}})^{1/2}$ . Upon entering the LN2-cooled section, vapor is assumed to condense on the walls creating an effective infinite boundary condition. The calculation proceeds as the droplets fall through the remining  $z_{\text{cooled}} = 0.85$  m distance resulting in a simulated physical time of

$$\Delta t = \left[ \left( v_{z,0}^2 + 2z_{cooled} g \right)^{1/2} - \left( v_0^2 + 2z_{ini} g \right)^{1/2} \right] / g.$$
 (18)

For the conditions considered here,  $\Delta t \approx 0.1$ s.

Figure 10 shows predicted results when a typical  $d_0 = 94 \,\mu\text{m}$  droplet is injected at  $v_{z,0} = 7.0 \,\text{m/s}$ . Results are shown for initial temperatures between  $T_0 = 0$  to 100 °C. As expected, evaporation leads to a predicted reduction in diameter (Figure 10a) as the droplets fall through the LN2-cooled section of the chamber. At the same time, transfer of latent heat from the droplet leads to evaporative cooling and droplet temperature decreases with distance (Figure 10b). As the temperature decreases the vapor pressure reduces (Figure 1) as does the rate of evaporation. By the downstream measurement location ( $z_d = 0.85 \,\text{m}$  in Figure 10) the predicted rate of change in diameter and temperature is vanishingly small for all conditions considered. This justifies the choice of measurement locations. Finally, note that the predicted change in diameter varies between 0 to ~10  $\,\mu$ m, which generally agrees with the range of diameter changes measured in the experiment (Table 1 and Figure 9).

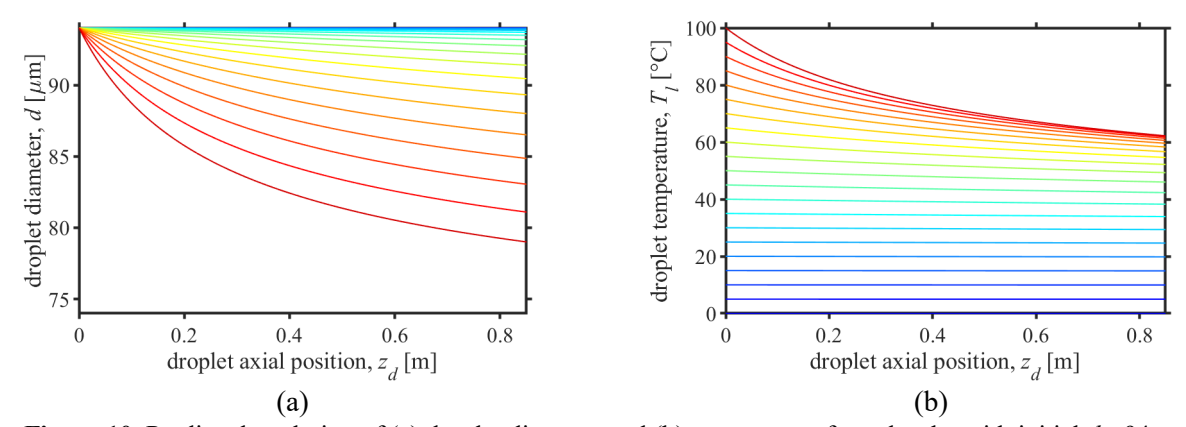
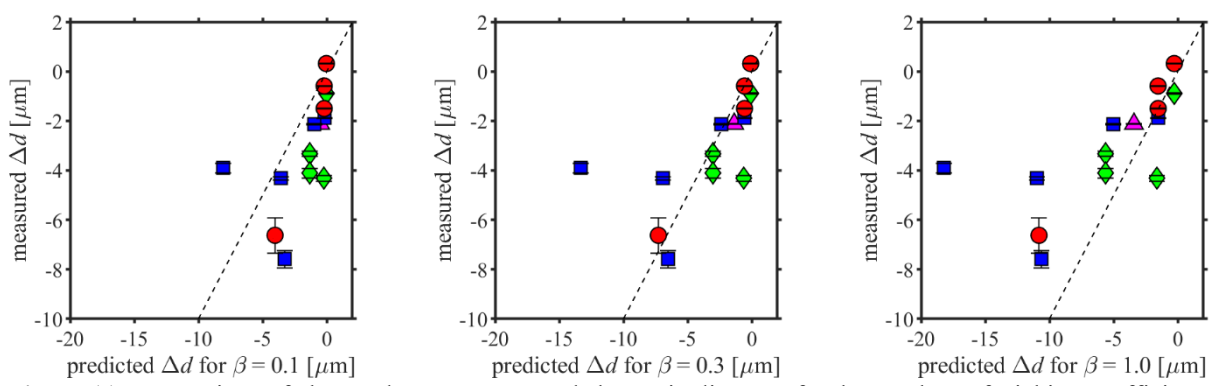


Figure 10. Predicted evolution of (a) droplet diameter and (b) temperature for a droplet with initial  $d_0$ =94 μm,  $v_{z,0}$  = 7.0 m/s, and  $T_0$  between 0 to 100 °C. Assumed  $\beta$  =0.3 for all curves. Line colors correspond to  $T_0$  given on the ordinate in (b).

To more quantitatively assess model accuracy, simulations are performed for every experimental data point for which a measured change in diameter is provided in Table 1. In each case the measured nozzle temperature, mean upstream diameter, and mean upstream vertical velocity define the initial conditions as described above. Figure 11 compares predicted changes in diameter on the abscissa with the measured changes in diameter on the ordinate. The sticking coefficient,  $\beta$ , is not well known *a priori*. For example, Nagayama and Tsuruta [30] defined a theoretical expression for  $\beta$  as

$$\beta = \left[1 - \left(n_{g,equil}/n_l\right)^{1/3}\right] \exp\left(\frac{-0.5}{\left(n_l/n_{g,equil}\right)^{1/3} - 1}\right).$$
(19)

Using the temperature dependent material properties in Eq. (1)-(2), the value of  $\beta$  predicted by Eq. (19) varies between 0.995 to 0.960 for the range of initial temperatures considered here. However, in more recent modeling and experiments considering organic molecules, Julin, Winkler, Donahue, Wagner and Riipinen [31] found  $\beta$  to span a much larger range from 0.1 to 1.0. Motivated by this, Figure 11 shows predicted results for three values of  $\beta$  between 0.1 to 1.0.



**Figure 11.** Comparison of observed versus computed change in diameter for three values of sticking coefficient,  $\beta$ , consistent with values of  $\beta$  found for organic liquids in Julin, Winkler, Donahue, Wagner and Riipinen [31]. See Figure 9 for legend.

Apart from the leftmost points, which are at the highest temperature, data in Figure 11 appear most consistent with a sticking coefficient of  $\beta \approx 0.3$  (when  $\beta$  is approximated as constant over the entire temperature range). This seems to indicate that the moderate values of  $\beta$  reported by Julin, Winkler, Donahue, Wagner and Riipinen [31] are more appropriate. Still, to more accurately quantify  $\beta$ , including potential variations of  $\beta$  as a function of temperature, more experimental data are needed, especially at higher initial temperatures.

Unfortunately, as discussed in the previous section, the horizontal spread of the droplet stream ultimately prevents accurate measures at higher initial temperatures. To elucidate the cause of the spreading, Figure 12 plots the measured standard deviation in horizontal droplet velocities for all experimental results in Table 1. Figure 12 results show minimal change in velocity fluctuations at the upstream location (blue dots) as a function of initial temperature. In contrast, at the downstream location (red dots) velocity fluctuations increase significantly at elevated temperatures. At a given temperature, the velocity changes shown in Figure 12 imply non-zero net forces acting on the droplets between the upstream and downstream location. When imparted over sufficient distance, these forces lead to the dispersion of the droplet stream observed at the downstream location.

Relatively few forces are known to cause droplets to repel from one another during flight. One possibility is electrostatic charge [32]. If the experimentally observed spread is due to droplet charging, the increased spread as a function of temperature would seem to suggest an effect from the electrical heater. To test this, the electrical feed was temporarily switched off while at elevated temperature. No changes in droplet velocity fluctuations were observed, indicating that electrostatic charge is unlikely. Alternatively, a stream of droplets may spread due to fluctuating drag forces exerted by the surrounding gas. Based on the theory of Reif [33] and reasonable assumptions for the molecular cross-section, at 80°C the viscosity of vapor phase DowTherm Q<sup>TM</sup> is estimated to be on the order of magnitude of 10<sup>-4</sup> Pa-s. Conservatively assuming the vapor environment in Figure 8 is fully saturated at 80 °C,

results in an estimated droplet Reynolds number on the order of 10<sup>-3</sup>. This is orders of magnitude less than Reynolds numbers where unstable wake behavior is typically observed. As a result, fluctuating drag forces are unlikely to contribute to the observed droplet spread.

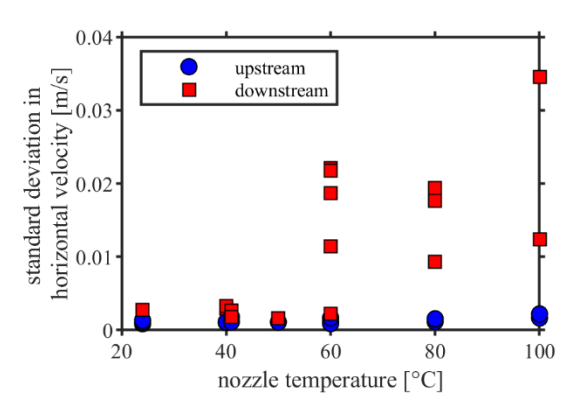


**Figure 12.** Comparison of the upstream and downstream experimentally measured standard deviation in droplet horizontal velocity.

Instead, it is hypothesized here that the spread observed at elevated temperatures is due to gas-phase forces imparted by absolute gradients in pressure and density. With vapor pressure greater than the ambient pressure, evaporation creates an elevated absolute pressure near the droplet stream. As the evaporated vapor spreads in the radial direction, the density and pressure decrease. Finally, at the surface of the LN2-cooled walls, the temperature is assumed to be much less than the freezing point of the liquid and vapor molecules are expected to condense with minimal rebound. This establishes a monotonically decreasing gradient in absolute pressure and density as a function of radius away from the centerline of the droplet stream. Consequently, any droplet, which is not exactly on the centerline at the upstream location, is subjected to a pressure gradient that tends to push the droplets away from the centerline as they propagate toward the downstream location. Because exact alignment is impossible, all drops experience some degree of pressure gradient. Furthermore, as the initial temperature of the liquid increases, the vapor pressure also increases (Figure 1). As a result, pressure gradients and the amount of droplet dispersion increase with initial droplet temperature.

For the experimental conditions considered here, the droplet Knudsen numbers, Kn, defined as the ratio of the molecular mean free path to the droplet diameter, is estimated to be on the order of 100 to 0.1, assuming saturated vapor environments between 20 to 100°C. These Kn correspond to the free molecular and traditional flow regimes [34]. At these rarified conditions, an initial estimate of the time averaged radial gas density profile created by the evaporating droplet stream is obtained by assuming no collisions and no gas reflected off boundaries. The number density in cylindrical coordinates r and z is calculated by adding the contribution to the gas density from droplets at axial positions  $z_d$ . From molecular flux conservation, the contribution from the i<sup>th</sup> droplet is

$$\frac{dn_g}{di} = n_{g,0} \frac{v_{gr,0} d^2}{4v_{gr} \left(r^2 + \left(z - z_d\right)^2\right)}$$
 (20)

Here,  $v_{gr}$  is the average radial velocity of gas molecules (relative to droplet) at radial position r and axial position z.  $n_{g,0}$  and  $v_{gr,0}$  are the number density and average radial velocity (relative to droplet), respectively, of gas molecules

emitted from the surface the droplet at r = d/2. Averaging Eq (20) over droplets spaced a distance a apart, the contribution to the gas density for droplets between  $z_d$  and  $z_d+dz_d$  is

$$\frac{dn_g}{dz_d} = \frac{n_{g,0}}{a} \frac{v_{gr,0} d^2}{4v_{gr} \left(r^2 + (z - z_d)^2\right)}$$
(21)

For gas distributions isotropic over a hemisphere,  $v_{gr} = v_{gr,0}[1+(1-d^2/4(r^2+(z-z_d)^2)^{1/2})] \approx 2v_{gr,0}$  for  $r^2+(z-z_d)^2 >> d^2/4$ . Assuming  $n_{g,0} \approx n_{g,equil}/2$  (only positive velocities are present at surface in vacuum) and integrating Eq (21) yields

$$n_{g}(r,z) \approx \int_{z_{d}=0}^{z_{d}=z_{f}} \frac{n_{g,equil}}{a} \frac{d^{2}}{16(r^{2}+(z-z_{d})^{2})} dz_{d}$$
 (22)

Here  $z_f$  is the furthest point in z from which gas may be evaporated from droplets. Equation (22) allows one to estimate the average density from the stream of droplets for at any r, z location. For r near the location of the droplet the density is approximately given by

$$n_{g}(r,z) \approx \frac{n_{g,equil}}{a} \int_{z_{d}=0}^{z_{d}=\infty} \frac{d^{2}}{16(r^{2} + (z - z_{d})^{2})} dz_{d} = \frac{n_{g,equil}d^{2}}{32ar} (\pi + 2 \tan^{-1}(z/r)) \approx \frac{\pi n_{g,equil}d^{2}}{16ar}$$
(23)

Equation (23) is approximately correct for r > d/2. Here, the integral is extended to infinity without significantly changing its value. In addition, temperature dependent variables are brought outside the integral, since the dominant contribution is from neighboring droplets, which are roughly at the same temperature.

To estimate the pressure gradient acting on the droplet it is assumed that  $T_g = T_l$ ,  $p_g = n_g k_b T_l$ , so that  $dp_g/dr = -\pi d^2 n_{g,equil} k_b T_l/(16ar^2)$  for r > d/2. For r < d/2, the pressure gradient is assumed to linearly increase matching the value at r = d/2 such that  $dp_g/dr \approx -\pi r n_{g,equil} k_b T_l/(2da)$  for r < d/2. It is further assumed that the force due to the pressure gradient is the only force acting on the droplet in the radial direction such that  $m_d(d^2r_d/dt^2) \approx -(\pi/4)d^3dp_g/dr$ , where  $m_d$  is the mass of the droplet and  $r_d$  is the radial position of the droplet. Combining with the above yields

$$\frac{d^2 r_d}{dt^2} = \frac{\pi^2 n_{g,equil} k_b T_i d^3}{64 m_d a} \begin{cases} \frac{2r_d}{d} & r_d < d/2 \\ \frac{d^2}{4r_d^2} & r_d > d/2 \end{cases}$$
(24)

Figure 13 shows the predicted mean horizontal extent of a steam of droplets with initial diameter of  $d_0 = 94 \,\mu\text{m}$  found by integrating Eq. (24). In this calculation, droplets are initialized with a horizontal displacement of one tenth of the droplet radius (4.7  $\mu$ m). Figure 13 results predict approximately zero spread when the droplets are initially at room temperature (20°C). At 50°C the predicted spread is on the order of a few mm. Finally, at 100°C the predicted spread is a few cm. This qualitatively matches the trends observed in Figure 5-Figure 8. Note that this calculation largely assumes the gas is collisionless, except where the perfect gas law is used to calculate pressure. Along the axis the density can be high so that a few collisions can occur in the distance of an inter-droplet separation (justifying the perfect gas law). At low densities this assumption overestimates the isotropization and the transverse pressure force. This strengthens the suggestion that there is large sensitivity to the density (and hence to the droplet temperature.)

In the experiments, accurate quantification of the miniscule initial droplet spread is challenging. In addition, at elevated temperatures, many of the droplets spread beyond the downstream field-of-view making quantification of the spread at the downstream location also challenging. Consequently, a more quantitative validation of this model is not currently possible. Nevertheless, this model and the experimental observations are consistent with the hypothesis of dispersion due to an absolute pressure gradient. Because very few, if any, experiments studying droplet evaporation at vacuum pressures have been reported in the literature, this may be the first time this mechanism has been observed, and previous assertions that droplet streams could be made to propagate in the vacuum of space for many kilometers without dispersion may need to be revisited [1,4].

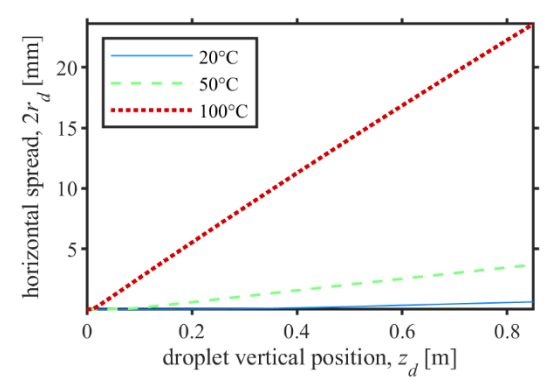


**Figure 13.** Horizontal extent of the spread in the droplet stream predicted by Eq (24) for three different temperatures Droplets are assumed to have an initial diameter of 94 μm and an initial horizontal displacement of 4.7 μm.

## **Summary and Conclusions**

This work presents an experimental and theoretical investigation of the transport and evaporation of a continuous stream of  $\sim 100~\mu m$  diameter liquid droplets in an environment initially evacuated at  $10^{-8}$  bar. The initial liquid temperature is heated between 25 to  $100^{\circ}$ C to vary the initial equilibrium vapor pressure between  $10^{-6}$  to  $10^{-3}$  bar. Droplets fall through a 0.8~m long section with liquid nitrogen cooled walls that simulate infinite radiation and vapor mass flux boundary conditions. At the lowest initial vapor pressure, experimental results show minimal droplet diameter change. At elevated initial vapor pressures, diameter changes of up to about 6  $\mu$ m are quantified. In addition, the stream becomes unstable and disperses in the radial direction.

Evaporation is modeled by the Hertz-Kundsen equation augmented with a temperature evolution equation. This formulation makes use of a theoretical sticking coefficient,  $\beta$ , to account for the fraction of vapor molecules that collide with and are absorbed into the liquid interface. Here, the predicted change in diameter is shown to best match the measured diameter changes for  $\beta \approx 0.3$  (when  $\beta$  is approximated as constant over the entire temperature range), indicating that the Hertz-Kundsen formulism gives qualitatively accurate results for values of  $\beta$  consistent with organic molecules.

Furthermore, theory is presented which attributes the spread in the droplet stream in the radial direction to forces exerted by an absolute pressure gradient created by the evaporating droplet stream. As demonstrated by the theory, when the initial vapor pressure is at the elevated conditions studied here, forces created by this pressure gradient are sufficient to disperse the droplets through the magnitude of the radial direction observed in experiments. Because of the uniqueness of the current experiment, this may be the first time this mechanism has been reported in

the literature, and previous assumptions that droplet streams will stably propagate over large distances in the vacuum of space may need to be revisited.

# Acknowledgements

The authors gratefully acknowledge Paul Farias, Rusty Spillers, Seth Spitzer, and Benjamin Halls of Sandia National Laboratories, Megan Paciaroni of Benedictine College, and Ellen Mazumdar of Georgia Tech for their assistance with the experimental configuration and analysis. This paper describes objective technical results and analysis. Any subjective views or opinions that might be expressed in the paper do not necessarily represent the views of the U.S. Department of Energy or the United States Government. Sandia National Laboratories is a multimission laboratory managed and operated by National Technology & Engineering Solutions of Sandia, LLC, a wholly owned subsidiary of Honeywell International Inc., for the U.S. Department of Energy's National Nuclear Security Administration under contract DE-NA0003525. Work performed at Lawrence Livermore National Laboratory under the auspices of the U.S. Department of Energy under contract DE-AC52-07NA27344.

#### References

- [1] E. Muntz and M. Orme, AIAA J. **25**, 746 (1987).
- [2] T. Totani, T. Kodama, H. Nagata, and I. Kudo, Journal of spacecraft and rockets 42, 493 (2005).
- [3] S. G. Tragesser, Journal of Guidance, Control, and Dynamics 32, 1277 (2009).
- [4] T. B. Joslyn, Ph.D., University of Colorado at Colorado Springs, 2010.
- [5] L. F. Velasquez-Garcia, A. I. Akinwande, and M. Martinez-Sanchez, Journal of Microelectromechanical Systems 15, 1272 (2006).
- [6] E. Muntz and M. Dixon, Dynamics of liquid droplets in the space environment, 1984.
- [7] K. D. Willis and M. E. Orme, Exp. Fluids **29**, 347 (2000).
- [8] T. Totani, T. Kodama, K. Watanabe, H. Nagata, and I. Kudo, Microgravity Science and Technology 17, 31 (2005).
- [9] A. F. Presler, C. E. Coles, P. S. Diem-Kirsop, and K. A. White III, Liquid droplet radiator program at the NASA Lewis Research Center, Report No. NASA TM-87139, 1985.
- [10] G. Konyukhov and A. Koroteev, Journal of Aerospace Engineering 20, 124 (2007).
- [11] H. Fuchs and H. Legge, Acta Astronautica 6, 1213 (1979).
- [12] Dow Chemical, DowTherm Q heat transfer fluid: product technical data, 1997.
- [13] Dow Chemical, DowThermQ heat transfer fluid material safety data sheet, 2015.
- [14] A. H. Lefebvre, Atomization and Sprays (Hemisphere Pub. Corp., New York, 1989).
- [15] D. P. DePonte, U. Weierstall, K. Schmidt, J. Warner, D. Starodub, J. C. H. Spence, and R. B. Doak, Journal of Physics D: Applied Physics 41, 195505 (2008).
- [16] Y. Hardalupas, S. Sahu, and A. M. Taylor, in 15th Int Symp on Applications of Laser Techniques to Fluid MechanicsLisbon, 2010).
- [17] L. Rayleigh, Proc. Lond. Math. Soc. **\$1-10**, 4 (1878).
- [18] T. D. Fansler and S. E. Parrish, Meas. Sci. Technol. 26, 012002 (2014).
- [19] D. Guildenbecher, J. D. Olles, T. J. Miller, P. L. Reu, J. D. Yeager, P. R. Bowden, and A. M. Schmalzer, in *International Detonation Symposium*Cambridge, Maryland, 2018).
- [20] D. R. Guildenbecher, M. A. Cooper, and P. E. Sojka, Applied Optics 55, 2892 (2016).
- [21] J. Gao, D. R. Guildenbecher, L. Engvall, P. L. Reu, and J. Chen, Applied Optics 53, G130 (2014).
- [22] D. R. Guildenbecher, J. Gao, P. L. Reu, and J. Chen, Applied Optics 52, 3790 (2013).
- [23] J. Gao, D. R. Guildenbecher, P. L. Reu, and J. Chen, Opt. Express 21, 26432 (2013).
- [24] D. Guildenbecher, W. M. Kunzler, W. C. Sweatt, D. R. Richardson, and K. M. Casper, Extending hypersonic diagnostics to the third dimension, Report No. SAND2017-9753R, 2017.
- [25] How can I determine my local values of gravitational acceleration and altitude? (FAQ Pressure), <a href="http://www.npl.co.uk/reference/faqs/how-can-i-determine-my-local-values-of-gravitational-acceleration-and-altitude-(faq-pressure)">http://www.npl.co.uk/reference/faqs/how-can-i-determine-my-local-values-of-gravitational-acceleration-and-altitude-(faq-pressure)</a> (Accessed November 2018).
- [26] H. Hertz, Annalen der Physik 253, 177 (1882).
- [27] M. Knudsen, Annalen der Physik **352**, 697 (1915).
- [28] A. H. Persad and C. A. Ward, Chem. Rev. 116, 7727 (2016).
- [29] J. Armijo and J. J. Barnard, Physical Review E 83, 051507 (2011).
- [30] G. Nagayama and T. Tsuruta, J. Chem. Phys. 118, 1392 (2003).

- [31] J. Julin, P. M. Winkler, N. M. Donahue, P. E. Wagner, and I. Riipinen, Environmental Science & Technology 48, 12083 (2014).
- [32] F. Sultan, N. Ashgriz, D. R. Guildenbecher, and P. E. Sojka, in *Handbook of Atomization and Sprays: Theory and Applications*, edited by N. Ashgriz (Springer, 2010).
- [33] F. Reif, Fundamentals of statistical and thermal physics (Waveland Press, 2009).
- [34] C. T. Crowe, Multiphase Flow Handbook (CRC Press, 2006).